LRP 661/00 January 2000

Microstructure and growth modes of stoichiometric NiAl and Ni3Al thin films deposited by rf-magnetron sputtering

P. de Almeida, R. Schäublin,
A. Almazouzi, M. Victoria, F. Lévy

Accepted in the Journal
THIN SOLID FILMS

ISSN 0458-5895

Microstructure and growth modes of stoichiometric NiAl and Ni_3Al thin films deposited by rf-magnetron sputtering

P. de Almeida*, R. Schäublin, A. Almazouzi, M. Victoria
CRPP-EPFL Fusion Technology Materials
CH-5232 Villigen PSI, Switzerland

F. Lévy
Institut de Physique Appliquée, EPFL
CH-1015 Lausanne, Switzerland

January 20, 2000

Abstract

Intermetallic thin films of stoichiometric NiAl and Ni_3Al have been deposited onto n-type silicon (100) and nickel (110) substrates using rf-magnetron co-sputtering. The morphology and crystal structure of the thin films have been studied by transmission electron microscopy from planar-view and cross-sectional samples. Chemical order has been assessed using nano-diffraction techniques. Superlattice reflections confirm a fully ordered structure in both intermetallics. These NiAl and Ni_3Al thin films are nanoscaled with an average grain size ranging from 50 to 100 nm and exhibit fiber textures in the $\langle 110 \rangle$ and $\langle 111 \rangle$ directions when deposited onto silicon. Granular- and heteroepitaxial relations have been observed when sputtering onto nickel at high substrate temperature. A granular-heteroepitaxial mode of growth exhibiting the inverse Nishiyama-Wassermann relation $(\bar{2}11)[\bar{2}11]_{B2} \parallel (\bar{1}10)[\bar{1}10]_{fcc}$ is observed in NiAl for the first time, whereas a single-crystalline heteroepitaxial growth relation of $(\bar{1}10)[\bar{1}10]_{L1_2} \parallel (\bar{1}10)[\bar{1}10]_{fcc}$ is achieved in Ni_3Al. The interface chemistry and surface topography have been studied by secondary ion mass spectroscopy and scanning tunneling microscopy, respectively, indicating an oxygen-free layer of very low surface roughness. The influence of the lattice matching and the deposition parameters on the thin film microstructure and orientation is discussed.

Ref: MS #99-0840

*Corresponding author. Tel.: +41-56-3104492; fax: +41-56-3104529; e-mail: Pedro.deAlmeida@psi.ch.

1 Introduction

In the Ni–Al system, thin film research is motivated by an increasing industrial interest to develop special coatings for advanced engineering applications, including low density wear-resistant materials, high-temperature structural materials [1,2] and state-of-the-art microelectronics, where interconnects and transition-metal aluminides on compound semiconductors are of paramount importance [3,4]. From a fundamental point of view these intermetallic thin films constitute interesting systems for the study of irradiation-induced phase transformations (order→disorder, amorphization) and defect production [5–9].

The growth of oriented crystals during condensation onto metallic substrates has been studied in the past decades for a great number of bilayer systems, namely for pure metals onto metals [10,11]. Research work has been published on the Ni-Al thin film deposition onto cleaved rock-salt [12–14], semiconductors [3,15], and in a limited scope onto nickel [2] where the thin film microstructure is transformed in a post-deposition annealing process. Although studies of the deposition conditions and its influence on the thin film crystalline structure and chemical composition exist [2,12–14], there is no systematic work relating these parameters to the thin film morphology, interface chemistry and epitaxial modes of growth.

Zone models [16,17], which used to predict the thin film microstructure as a function of primary deposition parameters such as the substrate temperature and the inert gas pressure, are quite useful for sorting out experimental results and for establishing starting points for the relationships between the physical vapor deposition (PVD) process and the microstructure. This approach is applied here in conjunction with a condensation regime analysis [18,19], which considers the surface energy balance between the substrate, the interface (transition layer) and the forming layer.

The major difficulties associated with the sputter deposition of intermetallic thin films are the control of the stoichiometry [20] and the growth of ordered individual grains in a stable superlattice microstructure [12]. This article reports on the synthesis and microstructural properties of rf-magnetron sputtered NiAl and Ni_3Al thin films onto n-type silicon (100) and nickel (110) substrates.

2 Experimental procedures

2.1 Thin film deposition

The NiAl and Ni_3Al thin films have been deposited in a sputtering system with two planar, confocal magnetron sources [21]. The most important deposition parameters are the target composition, working pressure, rf power, target-substrate distance, and especially the substrate

temperature, T_s. Two sputtering targets allow to control the chemical composition through calibration of their deposition rates. The alloy targets are homogeneous mixtures (hot-pressed) of $Ni_{75\ at.\%}Al_{25\ at.\%}$ and of $Ni_{50\ at.\%}Al_{50\ at.\%}$, with a purity of 99.9 at.%. A second target of nickel (purity 99.99 at.%) is used to adjust the chemical composition of the deposited film. The targets are water cooled discs, 50 mm in diameter, and controlled independently, making an angle of 5 degrees with respect to the substrate normal. Both intermetallics have been deposited onto silicon (100) and nickel (110) substrates in similar working conditions. The substrate temperature can be controlled from room temperature (RT) to about 800 K, using for this purpose a radiant heater placed behind the holder. Prior to the deposition the chamber was evacuated to a residual pressure of about 10^{-6} Pa, and backed out for 6 hours at 453 K. The target-substrate distance was fixed at 85 mm according to previous tests [21]. The substrate holder was rotating at 10 rpm. For T_s higher than RT the substrates were pre-heated for about 2 hours. The target power conditions during the deposition and the substrate temperatures are summarized in Table 1. The argon pressure during the deposition was 0.67 Pa. After five minutes pre-sputtering the deposition rate fluctuated by less than 5% indicating a steady-state of yield of the elemental constituents of the targets [22]. A calibration is presented in Fig. 1 for both materials. The use of a secondary nickel target hinders the plasma in the deposition chamber, due to its magnetic properties [23], and therefore reduces the total deposition rate by a factor of up to 20%. The main reason to co-sputter this element is to correct the thin film chemical composition around the stoichiometry within 1 to 2 at.%. Thickness measurements have been made in-situ using a Maxtek quartz crystal oscillator. The results were in good agreement with ex-situ measurements using an Alphastep stylus profiler. Test thicknesses between 200 nm and 1.5 μm were chosen for both NiAl and Ni_3Al as it is intended to irradiate the thin films with energetic ions and therefore their thicknesses should be in accordance with the projected range of the incoming ions.

2.2 Chemical analysis

Calibrated standards of single-crystalline samples of both intermetallics have been analyzed with conventional wet chemical tests. These results confirm the stoichiometric ratio and high-purity (99.999 at.%) of the samples and therefore will be used for comparisons with the thin films measured by X-Ray Energy Dispersive Spectrometry (EDS). Chemical analyses of the thin films and of the calibrated standards have been performed in a Philips XL30 FEG SEM using EDS. For the NiAl samples an acceleration voltage of 10 kV and a take-off angle of 35.8 degrees have been used. For the Ni_3Al samples an acceleration voltage of 15 kV has been used with the same take-off angle. A set of 3 different measurements per sample reproduced the same values within an accuracy better than 2 at.%, indicating that the films are chemically homogeneous (Table 2). These results are in agreement with the ones obtained for the single-crystals and therefore the

thin films are considered to have a stoichiometric chemical composition.

2.3 Measurement techniques

Cross-sectional specimens of NiAl and Ni_3Al thin films deposited onto nickel have been prepared with Focused Ion Beam (FIB) milling [24] due to the difficulties of mechanically polishing the metallic substrate down to a thickness of about 100 nm. The specimens are covered with a protective coating of gold and platinum to avoid sputtering of the intermetallic layer. They are cut and mounted onto copper rings and milled to the desired thickness using a gallium source operated at 30 keV.

Transmission electron microscopy (TEM) using a Philips CM20 operating at 200 kV has been used to investigate the general microstructure, the crystalline structure, texture and the chemical order (presence of superlattice reflections) using selected area diffraction (SAD) and nanodiffraction (ND). Cross-sectional samples have been observed using a JEOL 2010 operated at 200 kV.

Secondary ion mass spectroscopy (SIMS) measurements have been made with an Atomika 4000 apparatus, eroding an area of 100 μm $\times$ 100 μm by scanning an O_2^+ ion beam of 10 μm diameter at 10 keV.

Scanning tunneling microscopy (STM) has been performed with an Omicron apparatus operating in constant current mode after cleaning the samples in HF.

3 Results

3.1 Microstructure of thin film on silicon

A 0.5 μm thick NiAl thin film deposited onto silicon at 673 K and observed in a planar-view geometry [25] is seen to crystallize in a structure with grains of 60 nm in diameter (Fig. 2.a). The presence of Moiré fringes from overlapping grains indicate that several grains superpose along the film thickness. The structure is compact (no visible cavities at the grain boundaries) with individual grains well delimited by high-angle grain boundaries. The preferential growth in the $\langle 110 \rangle$ direction is confirmed by SAD (Fig. 2.c). When a planar-view specimen is tilted along a high-angle (Fig. 3.a) a quasi-cross sectional projection is observed, showing a structure with non-equiaxed (elongated) grains oriented along a preferential crystallographic direction perpendicular to the film substrate. These grains are 150 nm long and show interference fringes at the border. The morphology difference between these two regions of the same sample (in Fig. 2.a and Fig. 3.a) is due to nucleation and to the texturing effect, which develops a structure with small grains at the interface film/substrate and leads through coalescence to larger, elongated

grains. In agreement with the extended zone model of Movchan-Demchishin, for a reduced temperature T_s/T_m of 0.35, a regime of high surface diffusion (called Z2) becomes significant and drives columns having tight grain boundaries [10]. The bright-field/dark-field pair micrographs (Fig. 2.a and Fig. 2.b) confirm the typical grain size distribution, the Moiré interference fringes, and the well delimited grains with tight boundaries. The contrast distribution also indicates the texturing of the film (in the $\langle 110 \rangle$ direction). In SAD, spotty diffraction rings (Fig. 2.c) indicate that the thin film has grown with a fraction of elongated crystallites about 3 times larger than the average grain size. The chemical order is identified from ND patterns. The (100) and (111) superlattice reflections are clearly visible in this [011] zone axis ND (Fig. 3.b). These reflections are in agreement with those calculated for a NiAl crystal [26]. The lattice parameter determined from the ND pattern using a (200) reflection spot, a=0.287 nm, is in agreement with the bulk a=0.2887 nm [27].

For a 0.5 μm thick Ni_3Al thin film deposited onto silicon at 673 K, a bright-field/dark-field pair (Fig. 4.a and Fig. 4.b) shows that the grain size is 45 nm in average (Fig. 4.a) with poorly delimited grain boundaries (Fig. 4.b). The contrast indicates the existence of a defect structure, possibly stacking-faults, inside the crystallites (Fig. 5.a), and planes of crystallographic discontinuity at the grain boundaries [17]. The thin film is strongly textured in the $\langle 111 \rangle$ direction (Fig. 4.c). The spotty diffraction rings (Fig. 4.c) indicate large coalesced grains (about 100 nm). The reduced temperature (T_s/T_m) is in this case 0.4, and corresponds to a transition regime between ZT and Z2 [10]. In SAD patterns, (100) and (110) superlattice reflection are visible as the two diffraction rings close to the (111) ring (Fig. 4.c). The (100), (110), and (210) superlattice reflections are visible in a ND micrograph with a [001] zone axis (Fig. 5.c), in agreement with the simulated diffraction patterns. The existence of a (210) superlattice reflection identifies the crystal structure as being of type $L1_2$. The lattice parameter calculated from the (111) and (200) reflections, a=0.360 nm, is in agreement with the bulk value a=0.357 nm [27].

A cross-sectional view (details on the preparation available elsewhere [25]) shows the interface region between the silicon (100) substrate and the Ni_3Al thin film (Fig. 6.a) deposited with low growth rate at RT (in order to minimize the lattice mismatch strain [10]). The reduced temperature is 0.16, corresponding to a growth zone of type Z1 where the low deposition rate favors the development of a fiber texture morphology. In the SAD pattern the presence of satellites on the (111) diffraction ring (Fig. 6.b) indicates that the film is textured in the $\langle 111 \rangle$ direction. A bright-field/dark-field pair (Fig. 6.c and Fig. 6.d) evidences the structure of the thin film in cross-section with a sequence of stacking faults. The very fine interference Moiré fringes denote that the film is several grains in the thickness, possibly indicating micro twinning formation during deposition. A peak analysis from Fig. 6.b allows the detection of the (112) peak due to chemical order just before the (202) peak. The lattice parameter calculated from the (111) and the (112) diffraction rings, a=0.357 nm, is in agreement with the bulk value.

3.2 Microstructure of thin film on nickel

The microstructure of a 1.8 μm NiAl thin film deposited onto nickel (110) at high-temperature is shown in cross-sectional view tilted to a [112] ZA (Fig. 7.a). A subpopulation of the grains exhibit a granular-heteroepitaxial [11] inverse Nishiyama-Wassermann (NW) relationship $(\bar{2}11)[\bar{2}11]_{B2} \parallel (\bar{1}10)[\bar{1}10]_{fcc}$. This relation is established after analysis of the SAD pattern (Fig. 7.b) where the substrate diffraction vector $\vec{g_1} = 1/2[\bar{2}20]_{fcc}$ in a ZA=[112] is parallel to the thin film diffraction vector $\vec{g_1} = [\bar{2}11]_{B2}$ in a [111] ZA, being both perpendicular to the interface. Tilting the sample to a [110] ZA confirms the chemically ordered structure of the intermetallic by the presence of the {100}, {111} and {122} planes (h+k+l=odd). The reduced temperature (T_s/T_m) is 0.37, corresponding to a regime of type Z2. The lattice mismatch is 5.3%, being the lattice parameter ratio thin film to substrate equal to 0.8202. These values are in agreement with the optimal ratio and misfit limit defined in the rigid lattice approximation [28,29] for the NW orientation relation. This type of regime results in the microstructure being dominated by heteroepitaxially aligned grains due to the interface energy minimization of in-plane grain rotations [16]. The thin film is composed by grains exhibiting the inverse NW relationship and by polycrystalline grains of small size. As evaluated from the (110) reflections, the thin film lattice parameter, a=0.2886 nm, is in agreement with the bulk value.

The general microstructure of a 1.8 μm Ni_3Al thin film deposited onto nickel (110) at high-temperature is shown in cross-section (Fig. 8.a) tilted to a [112] zone axis (ZA). A heteroepitaxial growth relation of $(\bar{1}10)[\bar{1}10]_{L1_2} \parallel (\bar{1}10)[\bar{1}10]_{fcc}$ is established after the analysis of the SAD pattern (Fig. 8.b) where the substrate diffraction vector $\vec{g_1} = 1/2[\bar{2}20]_{fcc}$ is parallel to the single-crystalline thin film diffraction vector $\vec{g_1} = [\bar{1}10]_{L1_2}$ in a [112] ZA, being both perpendicular to the interface. The {110} family of planes (hkl, mixed even and odd) confirms the chemically structured phase of the intermetallic. The reduced temperature (T_s/T_m) is 0.4, and corresponds to a growth zone between types ZT and Z2. However, the lattice mismatch is minimal (1.4%) under the above mentioned orientation relation and therefore prompts a coherent growth. As evaluated from the (110) and the (220) reflections, the thin film lattice parameter, a=0.356 nm, is in agreement with the bulk value.

3.3 Interface characterization

The SIMS profile of a $Ni_{50.59\ \mathrm{at.\%}}Al_{49.41\ \mathrm{at.\%}}$ sample, 0.5 μm in thickness, deposited at 673 K on a silicon (100) substrate has been measured at an estimated average sputtering rate of 0.1 nm/s to a depth of about 0.8 μm (Fig. 9). The ratio of the oxygen background signal to the intensities of the elemental constituents is of the order of 10^{-4}. There is no significant increase of the oxygen content at the interface region. The depth resolution, which includes both the surface roughness and the cascade mixing, is estimated as 25 nm by fitting the trailing part of the intensity signal

of nickel-58 to a Gaussian distribution function of standard deviation σ, and assuming that this statistical value is one-half of the depth resolution [30–32].

The SIMS profile of a $Ni_{74.80\ at.\%}Al_{25.20\ at.\%}$ sample, 0.5 μm in thickness, deposited at 523 K on a silicon (100) substrate corresponds to a depth of about 0.7 μm with an average sputtering rate of 0.08 nm/s (Fig. 10). The relative intensity of the oxygen background to the elemental species of the thin layer is 1.40×10^{-4}. The depth resolution is estimated as 30 nm. The elemental signal intensity of both nickel and aluminum is constant throughout the deposited layer, thus indicating a homogeneous compound. The transition from a flat to a stiff slope in the elemental constituents intensities at the film interface indicates a non-diffused interface with an oxygen content almost as low as the sensitivity of the mass spectrometer.

3.4 Surface characterization

For the as-sputtered $Ni_{50.59\ at.\%}Al_{49.41\ at.\%}$ deposited at 673 K, the lateral grain size is in average 23 nm, with values as large as 50 nm (Fig. 11). The crystallites are formed by small subgrains with sizes ranging from 5 to 10 nm showing cavities between their boundaries, which is typical of a bcc crystalline lattice [21]. For the as-sputtered $Ni_{74.88\ at.\%}Al_{25.12\ at.\%}$ sample deposited at room temperature (RT), the lateral grain size is estimated as 36 nm (Fig. 12). The grains are well formed polygons delimited by high-angle grain boundaries, showing no cavities. The average surface roughness is in both cases of about 1 nm (Root Mean Square value).

4 Discussion

In contrast to earlier experiments [15], the present results show that the thin films deposited onto silicon (100) are polycrystalline with chemically ordered individual grains a few nanometers in typical size. Despite the small grain size, electron ND techniques allow to identify the superlattice reflection spots due to an ordered arrangement of the atomic sublattices. The strong lattice mismatch between the silicon substrate and the intermetallic thin films excludes the possibility of an epitaxial structure. Nevertheless, both films develop a specific two-dimensional texture as result of interfacial energy minimization between the substrate and the deposit in the early stages of nucleation [33], and because a crystal tends to expose surfaces having low Miller indices. These minimum stress surfaces correspond to the {110} lattice planes in a bcc structure and to the {111} planes in a fcc. They tend to orient parallel with the substrate plane during the growth. As observed with SAD, NiAl crystallizes in a bcc structure and Ni_3Al in a fcc. As expected, the preferential growth directions are the $\langle 110 \rangle$ and the $\langle 111 \rangle$. A three-dimensional island growth following the Volmer-Weber (VW) [10] mode induces a columnar structure ($d/t < 1$, where d and t are the characteristic linear dimensions of a non-equiaxed crystallite [16,34]) giving rise

to a fiber textured layer. This mechanism of nucleation is typically found during the growth of metals onto non-metallic substrates [35].

In an energy-enhanced deposition process like sputtering the impinging species reach the substrate with kinetic energies of the order of 1000 kJ/mol, higher than the chemical reaction energy [36,37], and are therefore adsorbed into the chemisorbed state (Eley-Rideal mechanism). Both aluminum and nickel have sputtering yields of the same order of magnitude [10]. This condition imposes an almost immediate steady state of atomic concentration in the deposit. As neither aluminum nor nickel have high atomic solubility into silicon at the substrate temperatures used, an abrupt interface forms between the substrate and the film, as it is indeed confirmed by SIMS and cross-sectional TEM observations. The substrate temperature can be kept high enough thus increasing the grain size of the thin film and enhancing structural order of the deposit through the mobility of the adatoms. Consequently, the polycrystalline intermetallic thin films are deposited with compositions close to the stoichiometric, being chemically ordered, textured, and showing great surface smoothness of the order of the nanometer.

The investigation of the microstructure and orientation in thin films of the intermetallic Ni–Al compounds deposited onto nickel (110) shows that: (a) NiAl exhibits an inverse NW granular-heteroepitaxial relationship, although this growth mode is mixed with a distribution of polycrystalline grains of small sizes. This mechanism can be understood as a dynamic balance between the surface energies γ_s, γ_f and γ_{in}, which stand for the substrate surface energy, the surface energy for a monolayer and the interface energy, respectively. Monolayer-by-monolayer growth occurs only in the Frank-van der Merwe (FvdM) [10] mode which is induced when $\Delta\gamma_n = \gamma_{fn} + \gamma_{in} - \gamma_s \leq 0$ for all n monolayers (thickness independent). This condition is fulfilled only in the case of homoepitaxy but can be partially satisfied in the heteroepitaxial case ($\gamma_s \neq \gamma_f$) until a given n-th monolayer. Beyond this point the mode of growth switches to Stranski-Krastanov (SK) [10] through the formation of three-dimensional crystals. The FvdM mode is achieved from the first monolayer, $\gamma_s = 2.364$ J/m^2 [38], $\gamma_f = 1.4$ J/m^2 [1], $\gamma_{in} \approx 0.746$ J/m^2 [1] and $\gamma_f + \gamma_{in} - \gamma_s = -0.218$ J/m^2. This layer-by-layer growth mode continues until the balance of the surface energies is no longer verified due to accumulation of strain energy (the lattice mismatch is 5.3%) leading to an increase of the interface energy. Assuming the rigidity modulus to scale with $\sqrt{n}$ this corresponds to a transition from FvdM to SK after the third monolayer. The energy mismatch, Γ_{sf}, is equal to 0.51. The ratio of the nearest-neighbor distances is 0.8202, which is in the range of values in order to eventually grow a layer in a NW orientation relationship with the substrate [28,29,38]; (b) Ni_3Al forms a single-crystalline layer and exhibits a heteroepitaxial relation of $(\bar{1}10)[\bar{1}10]_{L1_2} \parallel (\bar{1}10)[\bar{1}10]_{fcc}$. The nucleation mode is induced by a positive surface energy balance, $\Delta\gamma = \gamma_f + \gamma_{in} - \gamma_s > 0$, where $\gamma_f \approx 2.08$ J/m^2 [36,37] is the thin film surface energy for a monolayer, $\gamma_{in} \approx 1.2$ J/m^2 [39] is the interface energy and $\gamma_s = 2.364$ J/m^2 [38] is the substrate surface energy. A three-dimensional epitaxial island growth corresponding to a VW mode is achieved during the deposition process. The surface

energy mismatch, $\Gamma_{sf} = 2|(\gamma_s - \gamma_f)/(\gamma_s + \gamma_f)|$, is equal to 0.13. The critical value defined for the formation of a superlattice structure is $\Gamma_{sf} \leq 0.5$ [38]. Therefore, the growth of a superlattice structure is energetically favored.

A phase diagram has been established relating the deposition rate and substrate temperature of both intermetallics onto silicon (100) and nickel (110) to their thin film growth orientation (Fig. 13). The diagram shows, at deposition rates between 0.1 and 0.2 nm/s and substrate temperature below 300 K, the formation of polycrystalline intermetallic films onto silicon, whereas at low deposition rate and in a range of temperatures between 300 and 750 K a fiber texture develops. When the intermetallics are deposited onto nickel (110) single-crystals, a granular- and a heteroepitaxial mode of growth is evidenced.

5 Conclusions

The present results contribute to the systematic studies of the influence of the deposition parameters during the condensation of metallic elements onto semiconductors and metallic substrates and their influence on the thin film orientation. It demonstrates the heteroepitaxy of Ni_3Al and the inverse Nishiyama-Wassermann (NW) relationship observed for NiAl grown onto nickel (110). It shows that the observed orientation relations depend on the lattice parameter misfits, which are relatively small for the intermetallics onto nickel and therefore prompting a heteroepitaxial mode of growth. The nearest-neighbor distances ratio for NiAl onto nickel is close to the optimal values defined for the NW orientation relation of a bcc deposit onto a fcc substrate. This appears to be an indicator to predict the epitaxial growth of bcc-type intermetallic superlattices onto metallic substrates.

Acknowledgments

The present investigation was performed under a grant of the Swiss National Science Foundation (SNSF). The authors would like to thank Mr H. Jotterand and Mr A. Gentile, and Dr R. Sanjinés for their assistance in the preparation of the samples for rf-magnetron sputtering, and for the STM analyses made at the Institut de Physique Appliquée (EPFL). They would also like to acknowledge Dr O. Gebhardt for the SIMS measurements done at the Paul Scherrer Institut, Villigen. The electron microscopy of this work was performed partially at the Center of Microscopy (CIME) of the École Polytechnique Fédérale de Lausanne (EPFL). Dr F. Cléton (CIME) is duly acknowledged for the EDS measurements done.

References

[1] D. B. Miracle, Acta Metall. Mater. 41 (1993) 649.

[2] H. P. Ng, X. K. Meng, A .H. W. Ngan, Scripta Mater. 39 (1998) 1737.

[3] M. Ishida, S. Yuda, K. Kamigaki, H. Terauchi, S. Hiyamizu, N. Sano, Surf. Sci. 267 (1992) 54.

[4] J. M. E. Harper, K. P. Rodbell, J. Vac. Sci. Technol. B 15 (1997) 763.

[5] J. Eridon, G. S. Was, J. Mater. Res. 3 (1988) 626.

[6] K. K. Larsen, N. Karpe, J. Bøttiger, J. Mater. Res. 7 (1992) 861.

[7] M. Spaczér, A. Caro, M. Victoria, T. D. de la Rubia, Nucl. Instrum. Methods Phys. Research B102 (1995) 81.

[8] M. Spaczér, A. Caro, M. Victoria, Phys. Rev. B 52 (1995) 7171.

[9] M. Spaczér, A. Almazouzi, R. Schäublin, M. Victoria, Radiat. Eff. Def. Sol. 141 (1997) 349.

[10] D. L. Smith, Thin-Film Deposition: Principles and Practice, McGraw-Hill, Inc., New York, 1995.

[11] E. S. Machlin, The Relationships Between Thin Film Processing and Structure, vol. I, Giro Press, Croton-on-Hudson, N.Y., 1995.

[12] T. Kizuka, N. Mitarai, N. Tanaka, J. Mater. Sci. 29 (1994) 5599.

[13] D. Schryvers, M. Yandouzi, L. Toth, in: J. Boumendil, P. A. Buffat (eds.), Trinoculaire 98 des Microscopies, Strasbourg-Illkirch, France, July 01–July 03, 1998, pp. 31–32.

[14] M. Yandouzi, L. Toth, D. Schryvers, NanoStruct. Mater. 10 (1998) 99.

[15] H. Van Swygenhoven, H. Grimmer, F. Paschoud, M. Victoria, R. Hauert, NanoStruct. Mater. 4 (1994) 409.

[16] C. V. Thompson, Ann. Rev. Mater. Sci. 20 (1990) 245.

[17] J. A. Thornton, Ann. Rev. Mater. Sci. 7 (1977) 239.

[18] J. W. Matthews, (ed.), Epitaxial Growth: Part A, Academic Press, New York, 1975.

[19] J. W. Matthews, (ed.), Epitaxial Growth: Part B, Academic Press, New York, 1975.

[20] R. F. Bunshah, (ed.), Handbook of Deposition Technologies for Films and Coatings, second ed., Noyes Publications, New Jersey, 1994.

[21] W.-T. Wu, Ph.D. Thesis, Swiss Federal Institute of Technology Lausanne, Switzerland, 1996.

[22] D. A. Glocker, S. I. Shah, (eds.), Handbook of Thin Film Process Technology, Institute of Physics Publishing, Bristol, 1995.

[23] B. Window, F. Sharples, J. Vac. Sci. Technol. A 3 (1985) 10.

[24] K. Kuroda, M. Takahashi, T. Kato, H. Saka, S. Tsuji, Thin Solid Films 319 (1998) 92.

[25] K. P. G. Leifer, Ph.D. Thesis, Swiss Federal Institute of Technology Lausanne, Switzerland, 1997.

[26] P. A. Stadelmann, Ultramicroscopy 21 (1987) 131.

[27] O. Madelung, (ed.), Phase Equilibria, Crystallographic and Thermodynamic Data of Binary Alloys, Springer-Verlag, Berlin, 1991.

[28] J. H. van der Merwe, Phil. Mag. A 45 (1982) 145.

[29] O. Hellwig, K. Theis-Bröhl, G. Wilhelmi, H. Zabel, Thin Solid Films 318 (1998) 201.

[30] A. W. Czanderna, (ed.), Methods of Surface Analysis, Elsevier Scientific Publishing Company, Amsterdam, 1975.

[31] H. Liebl, J. Vac. Sci. Technol. 12 (1975) 385.

[32] S. Hofmann, J. Vac. Sci. Technol. B 10 (1992) 316.

[33] J. A. Szpunar, in: Steven M. Yalisove, Brent L. Adams, James S. Im, Yimei Zhu, Fu-Rong Chen (eds.), Polycrystalline Thin Films—Structure, Texture, Properties and Applications III, San Francisco, California, U.S.A., March 31–April 04, 1997, Materials Research Society Symposium Proceedings 472 (1997) 45.

[34] H. T. G. Hentzel, C. R. M. Grovenor, D. A. Smith, J. Vac. Sci. Technol. A 2 (1984) 218.

[35] R. W. Cahn, P. Haasen, E. J. Kramer, (eds.), Processing of Metals and Alloys, Materials Science and Technology, VCH, Basel, 1993.

[36] Y. Du, N. Clavaguera, J. Appl. Cryst. 237 (1996) 20.

[37] W. Huang, Y. A. Chang, Intermetallics 6 (1998) 487.

[38] E. Bauer, J. H. van der Merwe, Phys. Rev. B 33 (1986) 3657.

[39] G. Lu, N. Kioussis in: Steven M. Yalisove, Brent L. Adams, James S. Im, Yimei Zhu, Fu-Rong Chen (eds.), Polycrystalline Thin Films—Structure, Texture, Properties and Applications III, San Francisco, California, U.S.A., March 31–April 04, 1997, Materials Research Society Symposium Proceedings 472 (1997) 21.

Table 1: Thin film deposition parameters.

Sample Id.	T_s / K	Target No. 1	power / W	Target No. 2	power / W
NiAl/Si #1	673	$Ni_{50\ at.\%}Al_{50\ at.\%}$	80	Ni	15
Ni_3Al/Si #2	673	$Ni_{75\ at.\%}Al_{25\ at.\%}$	80	Ni	15
Ni_3Al/Si # 3	303	$Ni_{75\ at.\%}Al_{25\ at.\%}$	40	Ni	160
Ni_3Al/Si # 4	523	$Ni_{75\ at.\%}Al_{25\ at.\%}$	40	Ni	80
NiAl/Ni #H1	708	$Ni_{50\ at.\%}Al_{50\ at.\%}$	80	Ni	80
Ni_3Al/Ni #H2	675	$Ni_{75\ at.\%}Al_{25\ at.\%}$	80	Ni	80

Table 2: Chemical composition of the as-sputtered samples and of the intermetallic standards.

Sample Id.	Chemical composition	Analysis method
NiAl/Si #1	$Ni_{50.59\ at.\%}Al_{49.41\ at.\%}$	EDS
Ni_3Al/Si #2	$Ni_{73.71\ at.\%}Al_{26.29\ at.\%}$	EDS
Ni_3Al/Si #3	$Ni_{74.88\ at.\%}Al_{25.12\ at.\%}$	EDS
Ni_3Al/Si #4	$Ni_{74.80\ at.\%}Al_{25.20\ at.\%}$	EDS
NiAl X'tal #5	$Ni_{50.22\ at.\%}Al_{49.78\ at.\%}$	Wet-chemical
NiAl X'tal #6	$Ni_{52.43\ at.\%}Al_{47.57\ at.\%}$	EDS
Ni_3Al X'tal #7	$Ni_{74.82\ at.\%}Al_{25.18\ at.\%}$	Wet-chemical
Ni_3Al X'tal #8	$Ni_{73.79\ at.\%}Al_{26.21\ at.\%}$	EDS

Figure 1: Dependency of deposition rate versus target power for NiAl and Ni_3Al depositions.

Figure 2: NiAl thin film deposited at 673 K. (a) Bright-field (b) Dark-field under the (110) reflection (c) Selected area diffraction.

Figure 3: NiAl thin film deposited onto silicon at 673 K tilted to a high-angle. (a) Evidence of a non-equiaxed elongated grain structure (b) Nano-diffraction pattern (zone axis [011]).

Figure 4: Ni_3Al thin film deposited onto silicon at 673 K. (a) Bright-field (b) Dark-field under the (111) reflection (c) Selected area diffraction.

Figure 5: Ni_3Al thin film deposited onto silicon at 673 K. (a) Evidence of a defect pattern inside the crystallites (b) Nano-diffraction pattern (zone axis [001]).

Figure 6: (a) Cross-sectional view of the interface silicon/Ni_3Al thin film deposited at RT (b) Selected area diffraction (c) Bright-field of the thin-film region (d) Dark-field under the (111) reflection.

Figure 7: (a) Bright-field cross-sectional view of the interface 1.8 μm NiAl/nickel (110) bilayer deposited at 675 K (b) Selected area diffraction on the thin film region ([111] thin film ZA || [112] substrate ZA.)

Figure 8: (a) Bright-field cross-sectional view of the interface 1.8 μm Ni_3Al/nickel (110) bilayer deposited at 675 K (b) Selected area diffraction on the thin film region ([112] thin film ZA || [112] substrate ZA).

Figure 9: Secondary Ion Mass Spectrometry (SIMS) profile of a NiAl thin film deposited at 673 K.

Figure 10: Secondary Ion Mass Spectrometry (SIMS) profile of a Ni_3Al thin film deposited at 523 K.

Figure 11: Scanning Tunneling Microscopy (STM) analysis of the surface of a NiAl thin film deposited at 673 K.

Figure 12: Scanning Tunneling Microscopy (STM) analysis of the surface of a Ni_3Al thin film deposited at RT.

Figure 13: Thin film orientation as function of deposition rate and substrate temperature.

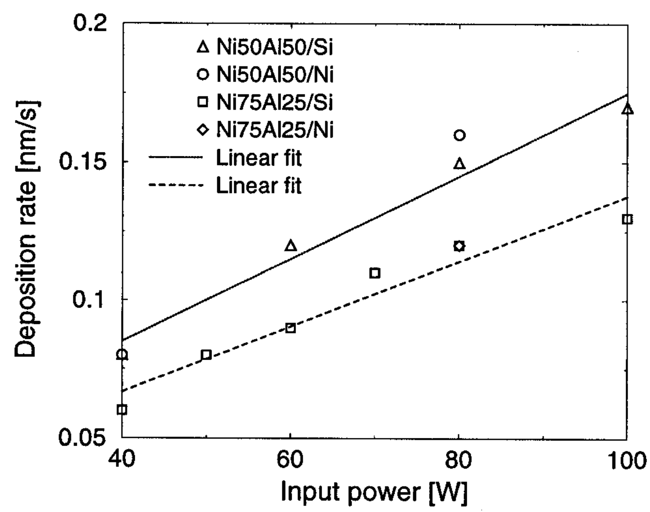

Fig. 1

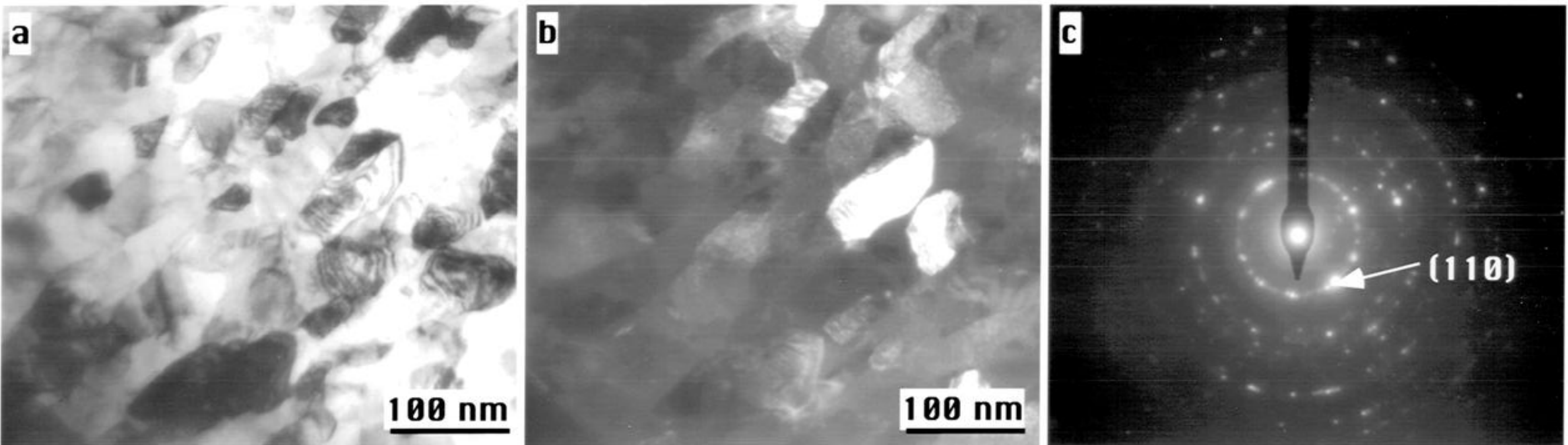

Fig. 2

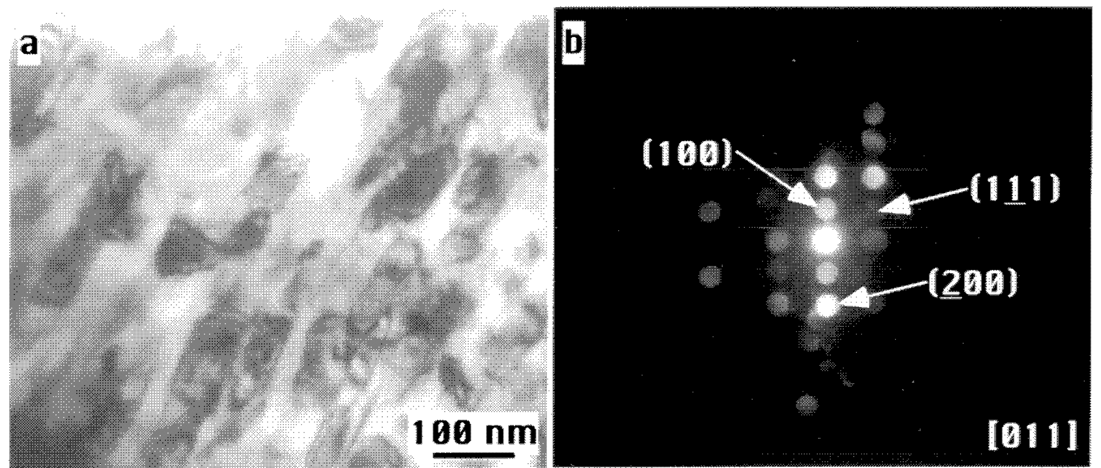

Fig. 3

19

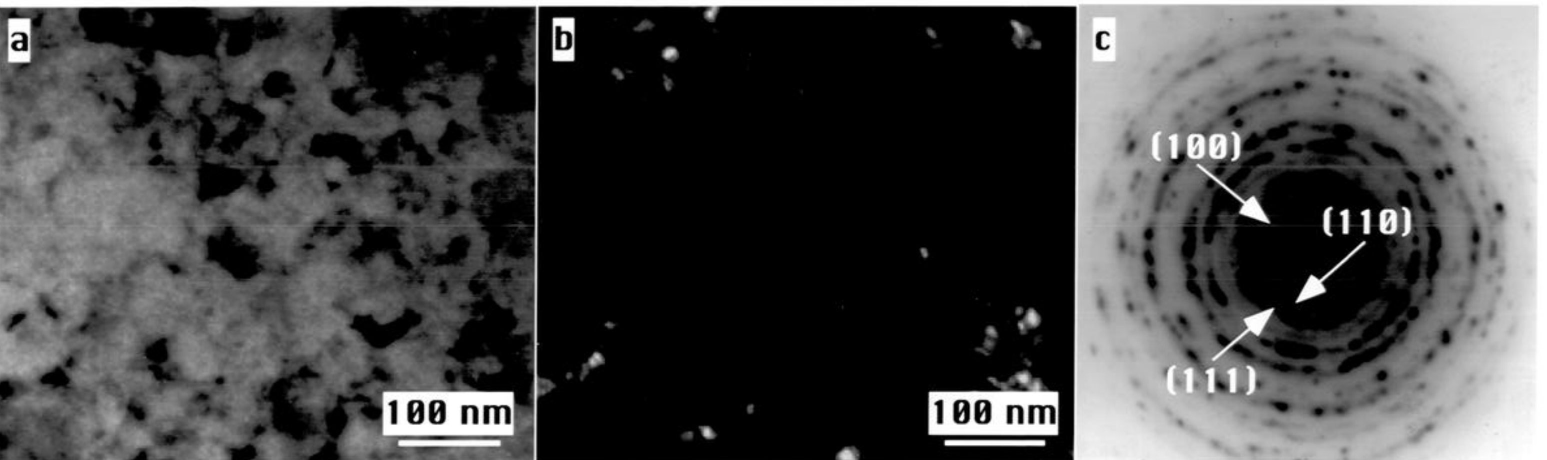

Fig. 4

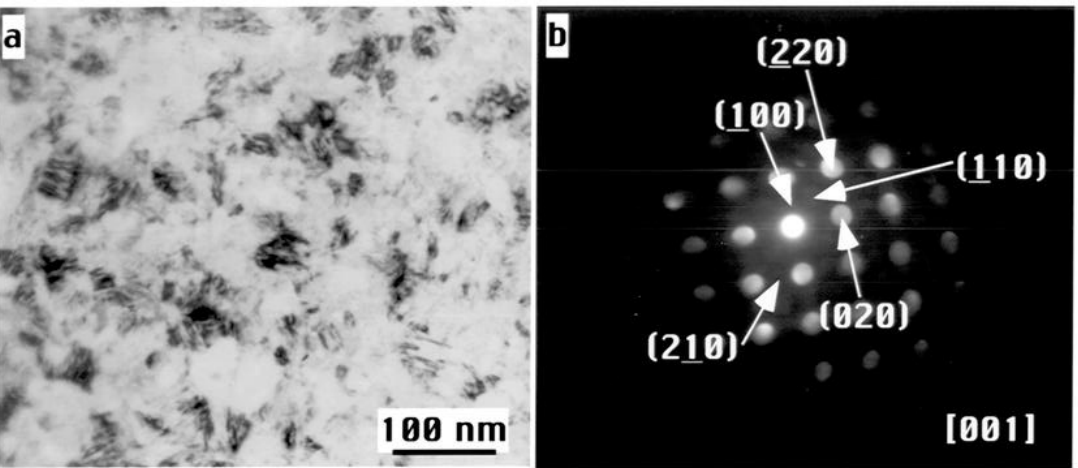

Fig. 5

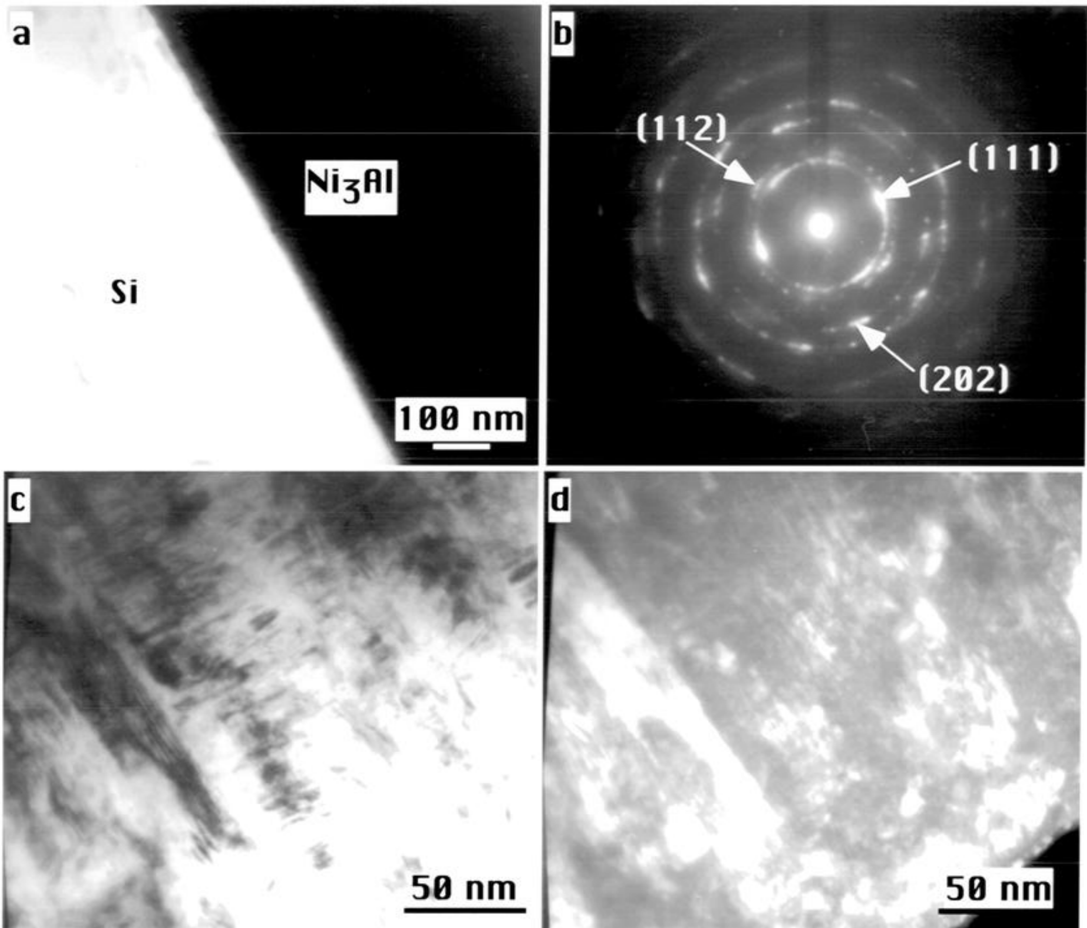

Fig. 6

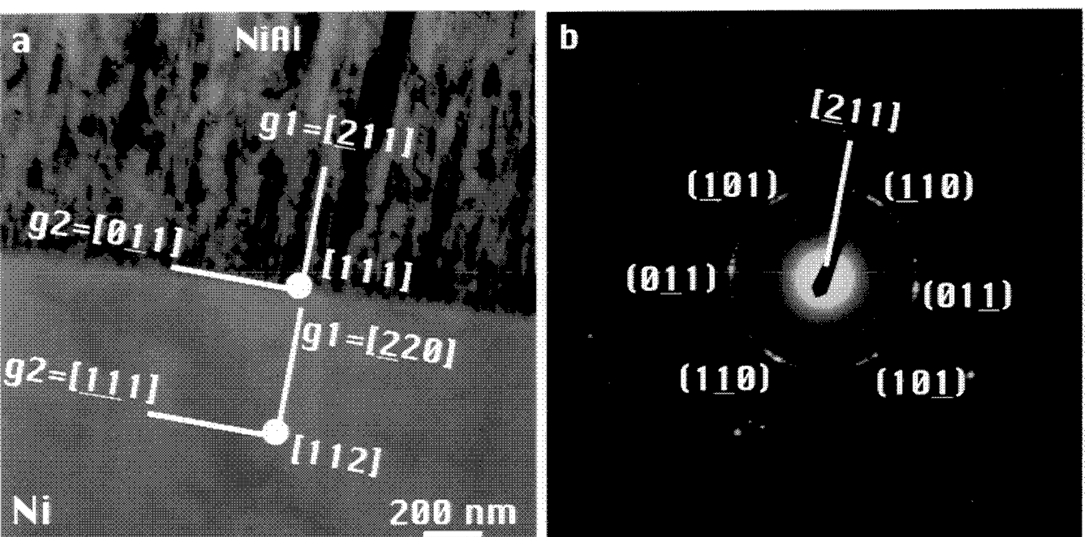

Fig. 7

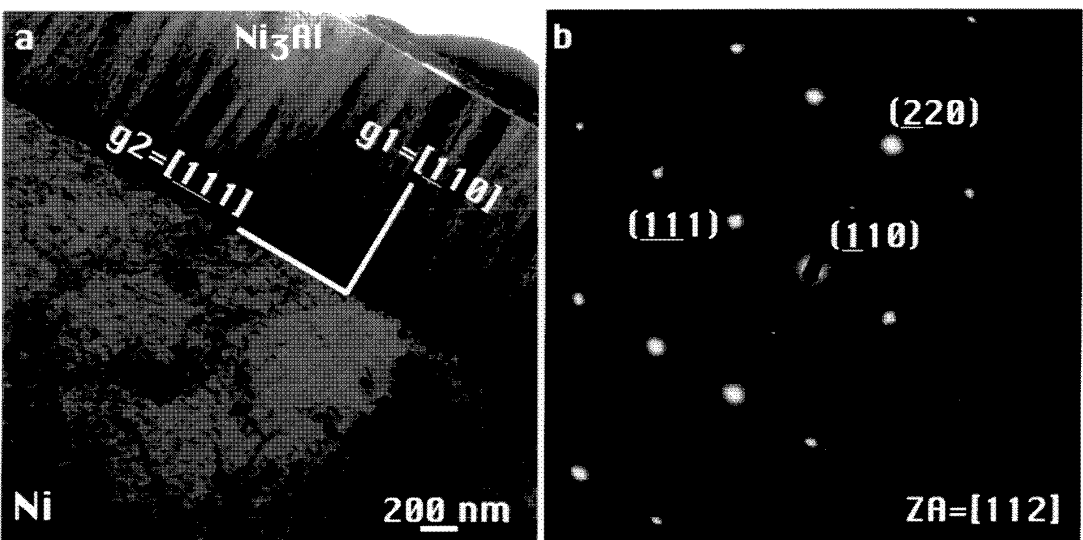

Fig. 8

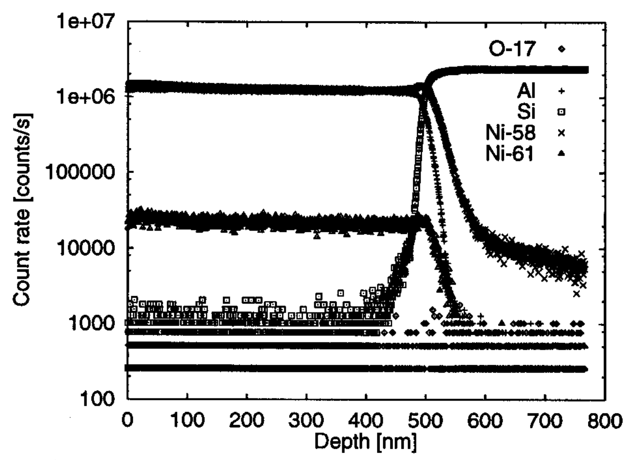

Fig. 9

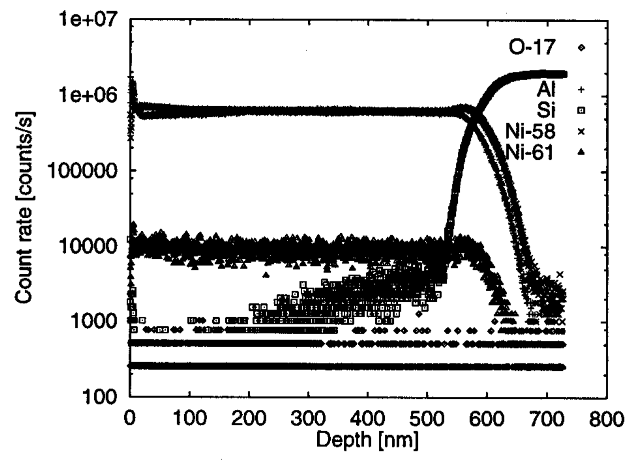

Fig. 10

Fig. 11

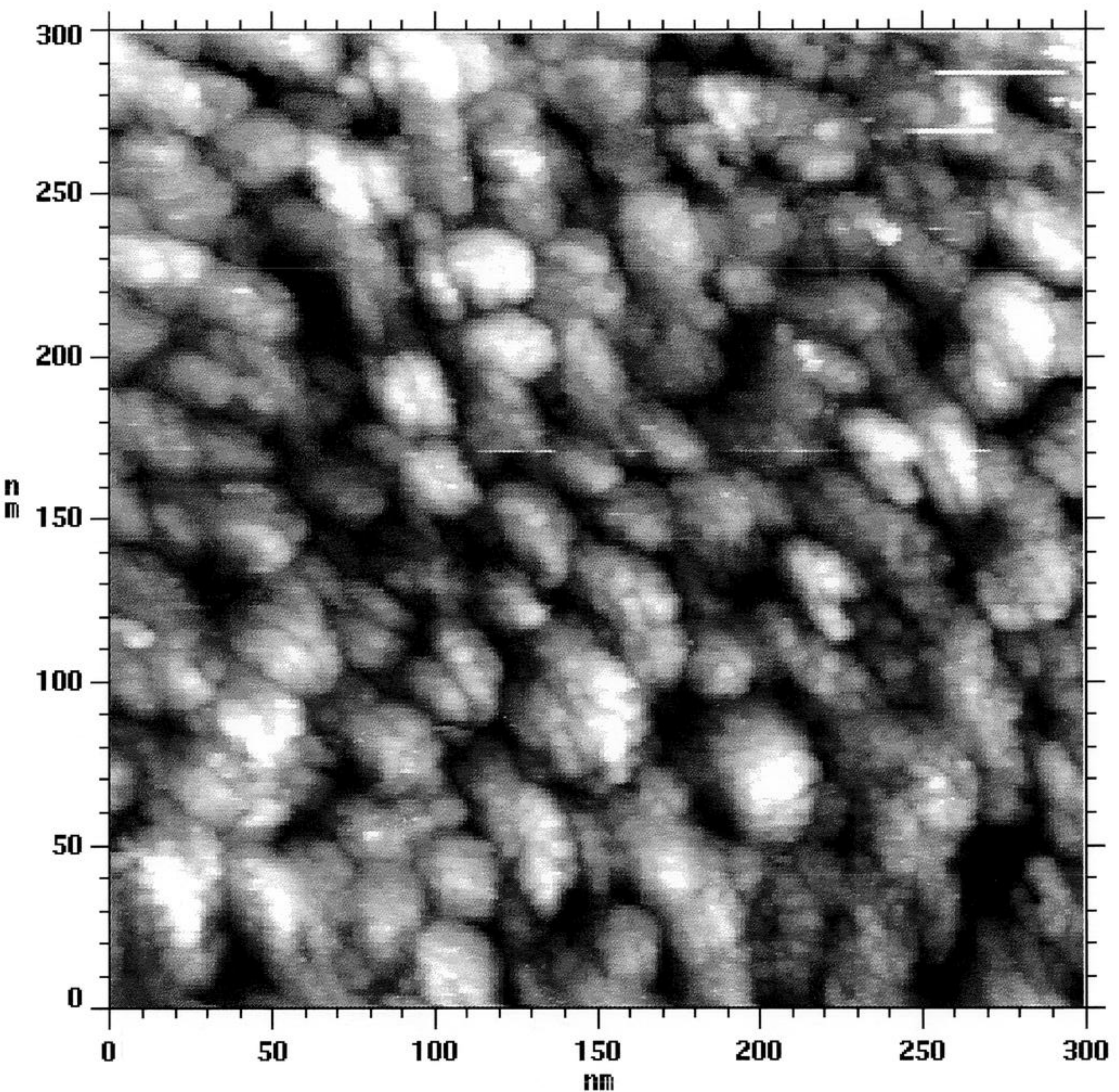

Fig. 12

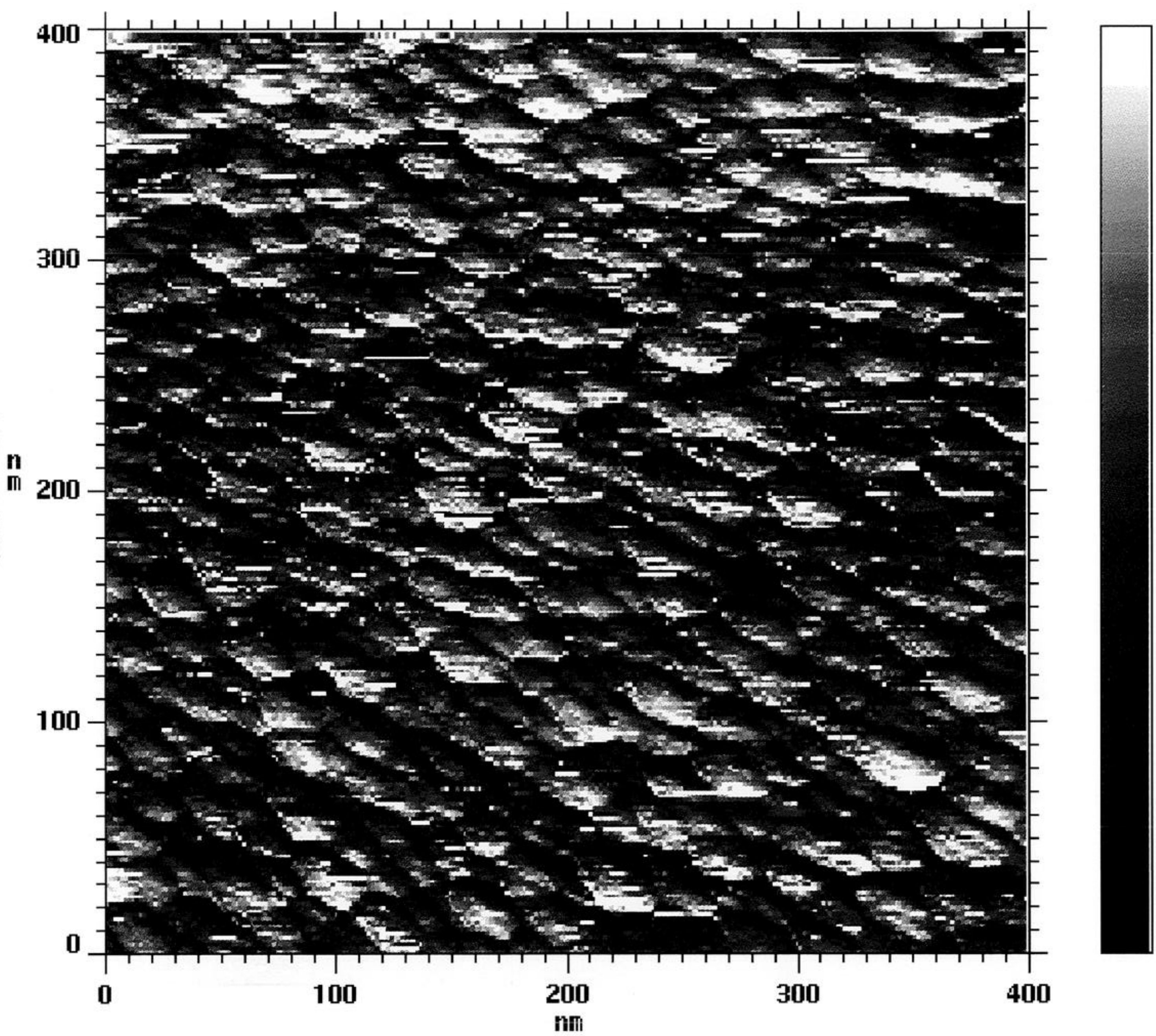

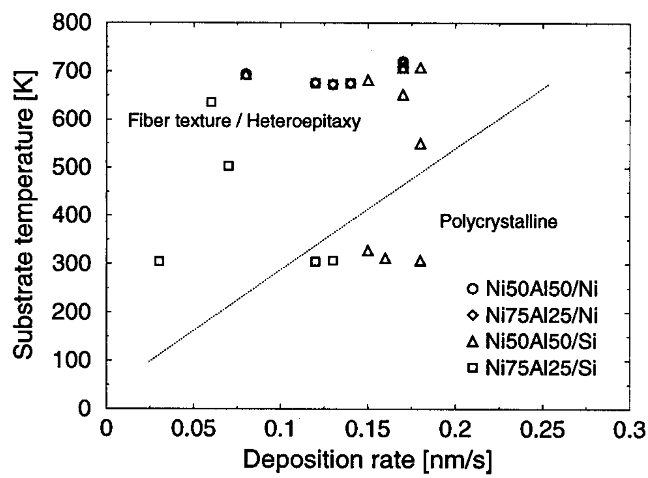

Fig. 13